Optimized tight binding between the S1 segment and KCNE3 is required for the constitutively open nature of the KCNQ1-KCNE3 channel complex

Go Kasuya[1]*, Koichi Nakajo[1]*

[1]*Division of Integrative Physiology, Department of Physiology, Jichi Medical University, 3311-1 Yakushiji, Shimotsuke, Tochigi, Japan 320-0498*

* Correspondence and requests for materials should be addressed to G.K. (gokasuya@jichi.ac.jp) and K.N. (knakajo@jichi.ac.jp).

Abstract

Tetrameric voltage-gated K^+ channels have four identical voltage sensor domains, and they regulate channel gating. KCNQ1 (Kv7.1) is a voltage-gated K^+ channel, and its auxiliary subunit KCNE proteins dramatically regulate its gating. For example, KCNE3 makes KCNQ1 a constitutively open channel at physiological voltages by affecting the voltage sensor movement. However, how KCNE proteins regulate the voltage sensor domain is largely unknown. In this study, by utilizing the KCNQ1-KCNE3-calmodulin complex structure, we thoroughly surveyed amino acid residues on KCNE3 and the S1 segment of the KCNQ1 voltage sensor facing each other. By changing the side-chain bulkiness of these interacting amino acid residues, we found that the distance between the S1 segment and KCNE3 is elaborately optimized to achieve the constitutive activity. In addition, we identified two pairs of KCNQ1 and KCNE3 mutants that partially restored constitutive activity by co-expression. Our work suggests that tight binding of the S1 segment and KCNE3 is crucial for controlling the voltage sensor domains.

Introduction

KCNQ1 (Kv7.1) is a voltage-gated K^+ channel. Its gating behavior depends mainly on its auxiliary subunit KCNE proteins (Wang et al., 2020). There are five KCNE genes in the human genome, and all of them are known to modify KCNQ1 channel gating behavior, at least in *Xenopus* oocytes or mammalian cell lines (Bendahhou et al., 2005). Therefore, the physiological functions of the KCNQ1 channel are determined by the type of KCNE proteins that are co-expressed in a tissue. The most well-studied example is the cardiac KCNQ1-KCNE1 channel, which underlies the slow cardiac delayed-rectifier K^+ current (I_{Ks}) (Barhanin et al., 1996; Sanguinetti et al., 1996; Takumi et al., 1988). Another example is the KCNQ1-KCNE3 channel, a constitutively open channel expressed in epithelial cells in the trachea, stomach, and intestine. This channel complex couples with some ion transporters to facilitate ion transport by recycling K^+ ions (Abbott, 2016; Grahammer et al., 2001; Preston et al., 2010; Schroeder et al., 2000).

The mechanisms by which KCNE proteins modify KCNQ1 channel gating behavior have been a central question of this ion channel. Since KCNQ1 is a classic shaker-type tetrameric voltage-gated K^+ channel, it has four independent voltage sensor domains (VSDs), one from each α subunit (Long et al., 2005). Each VSD consists of four transmembrane segments, S1-S4. Each S4 segment bears several positively charged amino acid residues. When the membrane potential is depolarized, each S4 segment moves upward (towards the extracellular side). That upward movement eventually triggers pore opening (Jensen et al., 2012; Larsson et al., 1996; Mannuzzu et al., 1996). Therefore, the S4 segment is considered to be an essential part of voltage-sensing (Aggarwal and MacKinnon, 1996; Catterall, 1988; Fedida and Hesketh, 2001; Liman and Hess, 1991; Logothetis et al., 1992; Noda et al., 1984; Papazian et al., 1991). As in the *Shaker* K^+ channel, the S4 segment of the KCNQ1 channel also moves upward with depolarization, as proved by scanning cysteine accessibility mutagenesis (SCAM) (Nakajo and Kubo, 2007; Rocheleau and Kobertz, 2008) and

voltage-clamp fluorometry (VCF) (Barro-Soria et al., 2014; Nakajo and Kubo, 2014; Osteen et al., 2012, 2010). In those studies, the presence of KCNE proteins was found to affect the voltage sensor movement. These results suggest that KCNE proteins stabilize a specific state during the voltage sensor transition (Barro-Soria et al., 2017, 2015, 2014; Nakajo, 2019). There should be at least three positions in the VSDs of KCNQ1: “down”, “intermediate”, and “up” (Hou et al., 2017; Taylor et al., 2020). KCNE1 stabilizes the intermediate position of VSDs along with a direct interaction of the pore domain and inhibits opening of the pore domain (Taylor et al., 2020). In contrast, KCNE3 may stabilize the intermediate or up position of VSDs and indirectly stabilize the channel's open state (Barro-Soria et al., 2017, 2015; Taylor et al., 2020). However, it remains unknown how KCNE proteins stabilize VSDs at a specific position.

Early studies by Melman *et al.* revealed “the triplet” of amino acid residues in the middle of the transmembrane segment (“FTL”: F57-T58-L59 in KCNE1 and “TVG”: T71-V72-G73 in KCNE3) as structural determinants of KCNE modulation properties (Melman et al., 2002, 2001). Exchanging the triplet (or one of the three amino acid residues) between KCNE1 and KCNE3 could introduce the other’s modulation properties, at least partially. For example, introducing “FTL” into KCNE3 transforms it into a KCNE1-like protein. Therefore, it has been long considered that “the triplet” is a functional interaction site between KCNQ1 and KCNE proteins. Possible interaction sites of the KCNQ1 side have also been explored and are believed to be located between the pore domain and the VSD (Chung et al., 2009; Kang et al., 2008; Nakajo and Kubo, 2007; Van Horn et al., 2011; Xu et al., 2008). By utilizing the KCNQ1 ortholog from ascidian *Ciona intestinalis*, which lacks KCNE genes, we previously found that F127 and F130 of the S1 segment are required for KCNE3 to make KCNQ1 a constitutively open channel (Nakajo et al., 2011). A recent computational model and the cryo-EM structure of the KCNQ1-KCNE3-calmodulin (CaM) complex clearly showed that KCNE3 interacts with the S1 segment and the pore domain (Kroncke et al., 2016; Sun and MacKinnon,

2020). However, the mechanism by which KCNE3 retains the KCNQ1 VSD at a specific position is still not clearly understood.

In this work, by taking advantage of the cryo-EM structure of the KCNQ1-KCNE3-CaM complex (Sun and MacKinnon, 2020), we created a series of the S1 segment and KCNE3 mutants to change the bulkiness of the S1 segment and KCNE3 interface and we found that the interaction between the S1 segment and KCNE3 is elaborately optimized to achieve the constitutive activity. In addition, we identified two pairs of the S1 segment and KCNE3 mutants that partially restored constitutive activity by co-expression. Our work suggests tight binding of the S1 segment and KCNE3 is crucial for controlling the voltage sensor domains.

Results

The side-chain volumes of amino acid residues in the S1 segment of KCNQ1 facing KCNE3 are optimized for channel modulation.

The cryo-EM structure of the KCNQ1-KCNE3-CaM complex revealed that KCNE3 interacts with the S1 segment of KCNQ1 in the transmembrane segment (Sun and MacKinnon, 2020). In the structure, the side chains of seven amino acid residues in the S1 segment of KCNQ1 (F123, F127, F130, L134, I138, L142, and I145) face lining those of six amino acid residues of the KCNE3 transmembrane segment (S57, I61, M65, A69, G73, and I76) (Figure 1). We previously reported that F127 and F130 are required to make KCNQ1-KCNE3 a constitutively open channel (Nakajo and Kubo, 2011). Therefore, we hypothesized that the interactions between the S1 segment of KCNQ1 and KCNE3 might be crucial for stabilizing the open states. To confirm the functional roles of these amino acid residues, we first created and tested small alanine and large tryptophan-substituted mutants of the S1 segment of KCNQ1. If the alanine and/or tryptophan-substituted mutants impaired the constitutive activity, we also created and tested intermediate-sized hydrophobic residues valine, leucine, and phenylalanine-substituted mutants. When expressed alone, most of the S1 segment mutants showed conductance-voltage (G-V) curves similar to that of KCNQ1 WT (Figure 2-figure supplements 1-7). We then tested how these mutations introduced to the S1 segment affect the modulation by KCNE3. When co-expressed with KCNE3 WT, KCNQ1 WT shifted the G-V curve in the far-negative direction, becoming a constitutively open channel for the physiological membrane potential range (Figure 2A, B, G, L; black traces and black G-V curves). Because of that, the relative conductance of KCNQ1 WT-KCNE3 WT at -100 mV ($\Delta G_{-100mV}/\Delta G_{max}$) was ten-times higher (KCNQ1 WT, 0.08 ± 0.01; KCNQ1 WT-KCNE3 WT, 0.80 ± 0.02; *n*=10 for each) (Figure 2M-S; black bars). In contrast, when co-expressed with KCNE3 WT, the S1 segment mutants yielded various G-V curves and $\Delta G_{-100mV}/\Delta G_{max}$ values. Since one of the unique features of the KCNE3

modulation is constitutive KCNQ1 activity even in the hyperpolarized voltage range, we then mainly evaluated the effect of each mutation on KCNE3 modulation by the $\Delta G_{-100mV}/\Delta G_{max}$ value for comparison. However, other parameters, such as the midpoint of the G–V curve ($V_{1/2}$) or effective charge (z), were evaluated when possible (table supplement 1). Both of the F123 mutants (F123A and F123W) shifted the G-V curves in the far-negative direction and kept the $\Delta G_{-100mV}/\Delta G_{max}$ values over 0.5 (F123A, 0.61 ± 0.01; F123W, 0.66 ± 0.01; *n*=10 for each) (Figure 2M-figure supplement 1), suggesting that the F123 residue did not have a large impact on the KCNE3 modulation. Among the F127 mutants (F127A, F127V, F127L, and F127W), F127A, F127V, and F127L mutants failed to shift the G-V curves in the far-negative direction and showed smaller $\Delta G_{-100mV}/\Delta G_{max}$ values depending on the side-chain size (F127A, 0.17 ± 0.02; F127V, 0.25 ± 0.02; F127L, 0.38 ± 0.02; *n*=10 for each) (Figure 2C-G, N-figure supplement 2). It seemed that the modulation depended on the side-chain volume: the more different the size was, the more significant was the impairment of modulation (Figure 2N). The F130 mutants (F130A, F130V, F130L, and F130W) failed to shift the G-V curves in the far-negative direction or even positively shifted the G-V curves. They showed substantially reduced $\Delta G_{-100mV}/\Delta G_{max}$ values (F130A, 0.02 ± 0.00; F130V, 0.10 ± 0.01; F130L, 0.01 ± 0.00; F130W, 0.37 ± 0.02; *n*=10 for each) (Figure 2O-figure supplement 3). Among the L134 mutants (L134A, L134V, L134F, and L134W), the L134A, L134V, and L134F mutants failed to shift the G-V curves in the far-negative direction and reduced the $\Delta G_{-100mV}/\Delta G_{max}$ values (L134A, 0.25 ± 0.01; L134V, 0.08 ± 0.01; L134F, 0.35 ± 0.02; *n*=10 for each) (Figure 2P-figure supplement 4). All the I138 mutants (I138A, I138V, I138F, and I138W) showed relatively mild attenuation in the G-V shift and $\Delta G_{-100mV}/\Delta G_{max}$ values (I138A, 0.36 ± 0.02; I138V, 0.66 ± 0.01; I138F, 0.64 ± 0.01; I138W, 0.36 ± 0.02; *n*=10 for each) (Figure 2Q-figure supplement 5). The I138 mutants showed an explicit size dependency in the KCNE3 modulation with wild-type isoleucine having the largest impact on the KCNE3 modulation, as in the case of the F127 mutants (Figure 2N). The L142 mutants (L142A,

L142V, L142F, and L142W) failed to shift the G-V curves in the negative direction and mildly reduced the $\Delta G_{-100mV}/\Delta G_{max}$ values (L142A, 0.24 ± 0.03; L142V, 0.42 ± 0.02; L142F, 0.60 ± 0.01; KCNQ1 L142W-KCNE3 WT, 0.23 ± 0.02; *n*=10 for each) (Figure 2R-figure supplement 6). Again, the L142 mutants showed an explicit size dependency in the KCNE3 modulation with wild-type leucine, as in the case of the F127 and I138 mutants (Figure 2N,Q,R). Among the I145 mutants (I145A, I145V, I145F, and I145W), smaller amino acid substitutions (I145A and I145V) were tolerable. In contrast, the I145F and I145W mutants positively shifted the G-V curves and reduced the $\Delta G_{-100mV}/\Delta G_{max}$ values as the side-chain size was increased (I145F, 0.11 ± 0.01; I145W, 0.03 ± 0.00; *n*=10 for each) (Figure 2H-L, S-figure supplement 7).

In summary, when mutated, six of seven tested amino acid residues (F127, F130, L134, I138, L142, and I145) in the S1 segment impaired the constitutive activity induced by KCNE3. Five of them (F127, F130, I138, L142, and I145) showed some side-chain volume dependency for the modulation by KCNE3: KCNQ1 WT showed the highest modulation effect by KCNE3, and the modulation effects by KCNE3 were gradually impaired if introduced mutations at the S1 segment became more different from WT in terms of amino acid size. Therefore, a series of side-chain volumes facing KCNE3 in the S1 segment is tightly optimized and vital for proper gating modulation of KCNQ1 induced by KCNE3.

The side-chain volumes of amino acid residues of KCNE3 facing the KCNQ1 S1 segment are also optimized for channel modulation

Next, we assessed the functional role of the six amino acid residues of KCNE3 facing the S1 segment (Figure 1). As in the case of evaluating the S1 segment, we created various mutants of these residues and co-expressed them with KCNQ1 WT. Throughout the experiments, 10 ng RNA of KCNQ1 was co-injected with 1 ng RNA of KCNE3 into oocytes since 1 ng RNA of KCNE3 was

sufficient to fully modulate KCNQ1 currents (figure supplement 8). In the S57 mutants (S57G, S57A, S57V, S57L, S57F, and S57W), the $\Delta G_{-100mV}/\Delta G_{max}$ values were more gradually reduced when introduced mutations became more different from WT, as seen in some S1 mutants (S57G, 0.32 ± 0.02; S57A, 0.66 ± 0.02; S57V, 0.47 ± 0.01; S57L, 0.20 ± 0.01; S57F, 0.10 ± 0.01; S57W, 0.10 ± 0.01; *n*=10 for each) (Figure 3A-G, N). Among the I61 mutants (I61G, I61A, I61V, I61F, and I61W), the I61V mutant reduced its $\Delta G_{-100mV}/\Delta G_{max}$ value to 0.57 ± 0.02 (*n*=10), but the value was still relatively high. The other four I61 mutants shifted the G-V curves in the positive direction and greatly reduced their $\Delta G_{-100mV}/\Delta G_{max}$ values (I61G, 0.04 ± 0.01; I61A, 0.03 ± 0.01; I61F, 0.04 ± 0.00; I61W, 0.11 ± 0.01; *n*=10 for each) (Figure 3O-figure supplement 9). The M65 mutants (M65G, M65A, M65V, M65L, M65F, and M65W) showed similar side-chain volume dependency as seen in the S57 mutants and some S1 mutants. They showed less shifted G-V curves and reduced the $\Delta G_{-100mV}/\Delta G_{max}$ values depending on how different the side-chain size was from that of WT, except M65V, which showed a large impairment of modulation despite having a size similar to that of WT (M65G, 0.22 ± 0.01; M65A, 0.48 ± 0.01; M65V, 0.16 ± 0.02; M65L, 0.63 ± 0.03; M65F, 0.36 ± 0.02; M65W, 0.07 ± 0.01; *n*=10 for each) (Figure 3P-figure supplement 10). Among the A69 mutants (A69G, A69V, A69L, A69F, and A69W), only the smaller A69G mutant was tolerated at this position. A69G shifted the G-V curve in the far-negative direction and kept the $\Delta G_{-100mV}/\Delta G_{max}$ value over 0.5 (0.57 ± 0.03, *n*=10), while the other four A69 mutants shifted the G-V curve in the positive direction and showed substantially smaller $\Delta G_{-100mV}/\Delta G_{max}$ values (A69V, 0.19 ± 0.02; A69L, 0.17 ± 0.01; A69F, 0.11 ± 0.01; A69W, 0.04 ± 0.01, *n*=10 for each) (Figure 3Q-figure supplement 11). Only the small amino acid alanine was tolerated again in the G73 mutants (G73A, G73V, G73L, G73F, and G73W) (Figure 3H-M,R). The G73A mutant shifted the G-V curve in the far-negative direction and kept the $\Delta G_{-100mV}/\Delta G_{max}$ value over 0.5 (0.77 ± 0.01, *n*=10). The other four G73 mutants mildly shifted the G-V curve in the negative direction and reduced the $\Delta G_{-100mV}/\Delta G_{max}$ values to variable

extents (G73V, 0.22 ± 0.02; G73L, 0.35 ± 0.02; G73F, 0.43 ± 0.02; G73W, 0.24 ± 0.01; *n*=10 for each) (Figure 3H-M,R). All of the I76 mutants (I76G, I76A, I76V, I76F, and I76W) showed reduced $\Delta G_{-100mV}/\Delta G_{max}$ values, depending on the side-chain volume (I76G, 0.06 ± 0.01, *n*=10; I76A, 0.14 ± 0.02, *n*=10; I76V, 0.43 ± 0.02, *n*=10; I76F, 0.11 ± 0.01, *n*=10; I76W, 0.16 ± 0.01; *n*=10 for each) (Figure 3S-figure supplement 12).

In summary, when mutated, all of the tested amino acid residues in KCNE3 showed some impairments in the modulation by KCNE3. Furthermore, KCNE3 WT showed the highest ability to modulate the KCNQ1 gating among all of the tested amino acid residues. In most cases, the abilities to modulate the KCNQ1 gating were more severely impaired if the size of introduced mutations differed more from WT. As in the case of the S1 segment (Figure 2-figure supplements 1-7), these results demonstrate that a series of side-chain volumes facing the S1 segment in KCNE3 is tightly optimized for proper gating modulation of KCNQ1 induced by KCNE3.

Functional restoration of the S1 mutants by the KCNE3 mutants

We then examined whether the KCNE3 mutations could restore the constitutive activity impaired by the S1 segment mutations. As guided by the KCNQ1-KCNE3-CaM complex structure (Sun and MacKinnon, 2020), we tested the idea with five candidate pairs positioned to the same layer in the structure (F127(Q1)-G73(E3), F130(Q1)-A69(E3), I138(Q1)-M65(E3), L142(Q1)-I61(E3), and I145(Q1)-S57(E3)) (Figure 1). In the F127(Q1)-G73(E3) pairs, we chose the KCNQ1 F127A mutant since it showed the largest impairment of KCNE3 modulation among the F127 mutants. Among the KCNE3 G73 mutants, the F127A-G73L pair showed the largest restoration of the $\Delta G_{-100mV}/\Delta G_{max}$ value (0.67 ± 0.01, *n*=10) as compared to that of the F127A-KCNE3 WT pair (0.17 ± 0.02, *n*=10) (Figure 4A-G). Other G73 mutants, G73V (0.36 ± 0.02, *n*=10), G73F (0.45 ± 0.02, *n*=10), and G73W (0.38 ± 0.01, *n*=10), also mildly but significantly restored the modulation (Figure 4A-G). In

the F130(Q1)-A69(E3) pairs, we examined whether KCNQ1 F130A and F130V mutants were restored by a series of the KCNE3 A69 mutants since they showed large impairments of KCNE3 modulation among the KCNQ1 F130 mutants. Although KCNE3 A69G, A69F, and A69W mutants slightly increaded the $\Delta G_{-100mV}/\Delta G_{max}$ value of the KCNQ1 F130A mutant (A69G, 0.10 ± 0.01; A69F, 0.05 ± 0.00; A69W, 0.10 ± 0.01; KCNE3 WT, 0.02 ± 0.00; *n*=10 for each), most of the KCNE3 A69 mutants failed to restore the KCNQ1 F130A and F130V mutants (figure supplement 13). In the I138(Q1)-M65(E3) pairs, we examined whether KCNQ1 I138A and I138W mutants were restored by a series of the KCNE3 M65 mutants since they showed large impairments of KCNE3 modulation among the KCNQ1 I138 mutants. In the KCNQ1 I138A-KCNE3 M65 pairs, the KCNQ1 I138A-KCNE3 M65L and KCNQ1 I138A-KCNE3 M65F pairs showed some restoration of the $\Delta G_{-100mV}/\Delta G_{max}$ values (KCNQ1 I138A-KCNE3 M65L, 0.52 ± 0.02, *n*=10; KCNQ1 I138A-KCNE3 M65F, 0.53 ± 0.01, *n*=10) as compared to that of the KCNQ1 I138A-KCNE3 WT pair (0.36 ± 0.02, *n*=10) (figure supplement 14A-H). The KCNQ1 I138W-KCNE3 M65L pair also showed mild restoration of the $\Delta G_{-100mV}/\Delta G_{max}$ value (0.46 ± 0.02, *n*=10) (figure supplement 14I-P), although it is not clear why both I138A and I138W were restored by the same M65L. In the L142(Q1)-I61(E3) pairs, we examined whether KCNQ1 L142A and L142W mutants were restored by a series of the KCNE3 I61 mutants. However, none of the pairs were restored (figure supplement 15). In the I145(Q1)-S57(E3) pairs, we examined whether KCNQ1 I145F and I145W mutants were restored by a series of the KCNE3 S57 mutants. Although the KCNQ1 I145W mutant was slightly restored by the KCNE3 S57 mutants, no KCNE3 S57 mutants showed a $\Delta G_{-100mV}/\Delta G_{max}$ value higher than 0.18 (figure supplement 16). In contrast, KCNQ1 I145F was successfully restored by KCNE3 S57G and S57A mutants with smaller residues than WT ($\Delta G_{-100mV}/\Delta G_{max}$ values of I145F-S57G, 0.43 ± 0.01; I145F-S57A, 0.61 ± 0.02; *n*=10 for each) as compared to that of the I145F-KCNE3 WT pair (0.11 ± 0.01, *n*=10) (Figure 4H-O).

These results suggest that at least two of the five pairs of residues tested (F127(Q1)-G73(E3) and I145(Q1)- S57(E3)) closely interact with each other, which further strengthens the importance of the tight interaction between the S1 segment and KCNE3.

The KCNE3 mutants restored impaired voltage sensor movement of the S1 mutants

Previous electrophysiological studies demonstrated that KCNE3 influences the voltage sensor movement, especially the S4 segment movement (Barro-Soria et al., 2017, 2015; Nakajo and Kubo, 2007; Rocheleau and Kobertz, 2008). We next performed VCF to monitor the S4 segment to investigate whether voltage sensor movement is impaired by the mutations of the S1 segment and whether it is restored by the identified pairs of mutants (F127A(Q1)-G73L(E3) and I145F(Q1)-S57A(E3)). The KCNQ1 channel for VCF (KCNQ1 C214A/G219C; this construct hereafter being referred to as "$KCNQ1_{vcf}$ WT") was labeled at the introduced cysteine residue (G219C) by Alexa Fluor 488 maleimide (Osteen et al., 2012, 2010). Currents and fluorescence changes in response to voltage steps (from 60 to -160 mV) from a holding potential of -100 mV were recorded (Figure 5 inset). $KCNQ1_{vcf}$ WT alone showed a fluorescence-voltage (F-V) relationship that mostly fitted to a single Boltzmann function and closely overlapped with its G-V curve (figure supplement 17A,D,E). In contrast, $KCNQ1_{vcf}$ WT co-expressed with KCNE3 WT showed a split F-V relationship. Its fluorescence changes were observed in the far negative and positive voltages, while they were very small and remained almost unchanged within the voltage range between 0 and -100 mV (Figure 5A,F,G). Consequently, the F-V relationship of $KCNQ1_{vcf}$ WT-KCNE3 WT does not fit to a single Boltzmann function but fits to a double Boltzmann function (Figure 5A,F,G), which is consistent with the results of a previous VCF study (Taylor et al., 2020). These results suggest that most of the S4 segments of the channels are at the down position and move to the upper position with depolarization in $KCNQ1_{vcf}$ WT alone and that a substantial number of S4 segments

are in the intermediate position and move either with depolarization or deep hyperpolarization in $KCNQ1_{vcf}$ WT-KCNE3 WT. We then assessed the F-V relationships of the $KCNQ1_{vcf}$ F127A mutant co-expressed with the KCNE3 WT or G73L mutant as well as those of the $KCNQ1_{vcf}$ I145F mutant co-expressed with the KCNE3 WT or S57A mutant. The $KCNQ1_{vcf}$ F127A and F145F mutants alone showed G-V and F-V relationships similar to those of $KCNQ1_{vcf}$ WT alone (figure supplement 17B-E). The $KCNQ1_{vcf}$ F127A mutant co-expressed with KCNE3 WT showed an F-V relationship that still fitted to a double Boltzmann function but lost a plateau phase observed in $KCNQ1_{vcf}$ WT-KCNE3 WT (Figure 5B,G), resulting in a shift of the half-activation voltage in the first fluorescence component ($V_{1/2(F1)}$), which seems to be correlated to pore opening/closure, toward the positive direction (-77.1 ± 3.0 mV, *n*=5) as compared to that of $KCNQ1_{vcf}$ WT-KCNE3 WT (-141.7 ± 10.8 mV, *n*=5). In contrast, the $KCNQ1_{vcf}$ F127A mutant co-expressed with the KCNE3 G73L mutant showed an F-V relationship that better fitted to a double Boltzmann function and shifted its $V_{1/2(F1)}$ toward a more negative direction (-175.3 ± 27.3 mV, *n*=5) than the $KCNQ1_{vcf}$ F127A mutant co-expressed with KCNE3 WT (Figure 5C,G). These results suggest that the number of S4 segments in the intermediate position were increased in the $KCNQ1_{vcf}$ F127A mutant co-expressed with the KCNE3 G73L mutant.

A similar tendency was observed in the $KCNQ1_{vcf}$ I145F mutant co-expressed with the KCNE3 WT or S57A mutant (Figure 5D,E,I). The $KCNQ1_{vcf}$ I145F mutant co-expressed with KCNE3 WT showed an F-V relationship that still fitted to a double Boltzmann function but lost a plateau phase and shifted its $V_{1/2(F1)}$ toward the positive direction (-121.2 ± 11.6 mV, *n*=5). In contrast, the $KCNQ1_{vcf}$ I145F mutant co-expressed with the KCNE3 S57A mutant showed an F-V relationship that better fitted to a double Boltzmann function and shifted its $V_{1/2(F1)}$ toward a more negative direction (-173.8 ± 11.2 mV, *n*=5). These results suggest that the number of S4 segments in the intermediate position were increased in the $KCNQ1_{vcf}$ I145F mutant co-expressed with the KCNE3

S57A mutant.

Overall, the results indicate that KCNE3 residues in the middle of the transmembrane segment are important for channel modulation, probably by preventing the S4 segment from going to the down position.

Discussion

In this work, we conducted site-directed mutational analyses using TEVC and VCF, inspired by the recently determined cryo-EM structures of the KCNQ1-KCNE3-CaM complex (Sun and MacKinnon, 2020). We found that the hydrophobic interface between the S1 segment and KCNE3 is a key component for the channel modulation by KCNE3, which prevents the S4 segment of the VSD from going to the down position at resting membrane potential.

Previous studies demonstrated that “the triplet” of amino acid residues in the middle of the transmembrane segment (“FTL” for KCNE1 and “TVG” for KCNE3) is a structural determinant of KCNE modulation properties (Barro-Soria et al., 2017; Melman et al., 2002, 2001). However, why the triplets are important for conferring specific gating properties onto KCNQ1 is still not well understood even though the KCNQ1-KCNE3-CaM complex structure revealed that the triplets are located deep inside the membrane and interact with the S1 and S4 segments of KCNQ1 (Sun and MacKinnon, 2020) (Figure 1A). Besides “the triplet,” our current work showed that a broader range of amino acid residues (S57, I61, M65, A69, G73, and I76), which forms five helical turns in total in the middle of the transmembrane segment of KCNE3, were involved in the interactions between KCNE3 and the S1 segment and were required for maintenance of constitutive activity of the KCNQ1-KCNE3 channel (Figure 3-figure supplements 9-12).

Another previous study by Barro-Soria *et al.* suggested that negatively charged KCNE3 residues (D54 and D55) electrostatically interact with the S4 segment of KCNQ1 to induce constitutive activity of the KCNQ1-KCNE3 channel (Barro-Soria et al., 2015). In this work, we did not investigate these negatively charged KCNE3 residues since they are far away from the S1 and S4 segments and do not directly interact with them in the KCNQ1-KCNE3-CaM complex structure (Sun and MacKinnon, 2020). Further mutational analyses can provide insights into the mechanism of how these residues are involved in gating modulation of KCNQ1 induced by KCNE3.

For the KCNQ1 side, we previously demonstrated that two phenylalanine residues, F127 and F130, in the S1 segment are important for the channel modulation by KCNE3, but how these mutations affect the channel modulation has been unknown (Nakajo et al., 2011). The cryo-EM KCNQ1-KCNE3-CaM structure (PDB: 6V00) clearly shows that F127 and F130 of the S1 segment face KCNE3 (G73 and I76). We therefore hypothesized that the interaction of these amino acid residues is essential for the KCNE3 function and found that besides F127 and F130, a broader range of amino acid residues (F127, F130, L134, I138, L142, and I145), which forms five helical turns in total in the middle of the transmembrane segment of the S1 segment, were important for the channel modulation by KCNE3. Furthermore, in most cases, the introduction of larger and smaller amino acid residues at the hydrophobic interface between the S1 segment and KCNE3 disrupted the KCNE3 function to modulate KCNQ1 gating (Figure 2-figure supplements 1-7). This suggests that the side-chain volume of the amino acid residues in the S1 segment and KCNE3 is optimized for proper gating modulation of KCNQ1 induced by KCNE3 (Figures 2 and 3-figure supplements 1-7,9-12). The restorations of the KCNQ1 F127A mutant by the KCNE3 G73L mutant and the KCNQ1 I145F mutant by the KCNE3 S57A mutant further support this idea (Figure 4). In contrast, three of the five KCNQ1 residues tested (F130, I138, and L142) were not successfully restored by KCNE3 mutants (figure supplements 13-15). They could have even more prominent roles in the KCNE3 modulation than just the tight hydrophobic interaction tested in this study. Further analyses are needed to understand the functions of these residues in gating modulation by KCNE3.

According to previous VCF studies (Barro-Soria et al., 2017, 2015; Taylor et al., 2020), we further performed VCF analysis to investigate how the S1 segment and KCNE3 interaction influences the voltage sensor movement. Previous VCF analysis (Taylor et al., 2020) revealed that $KCNQ1_{vcf}$ WT co-expressed with KCNE3 WT showed two components (F1 and F2) in the F-V relationship (Figure 5A,F,G). In addition, $KCNQ1_{vcf}$ F127A-KCNE3 WT and $KCNQ1_{vcf}$ I145F-KCNE3 WT pairs

showed positively shifted $V_{1/2(F1)}$ and diminished the plateau phase observed in the $KCNQ1_{vcf}$ WT-KCNE3 WT pair, while $KCNQ1_{vcf}$ F127A-KCNE3 G73L and $KCNQ1_{vcf}$ I145F-KCNE3 S57A pairs partially restored $V_{1/2(F1)}$ and the plateau phase (Figure 5). These results suggest that the tight interaction between the S1 segment and KCNE3 is required to keep the S4 segment in the intermediate position at resting membrane potential. Disrupting the interaction between the S1 segment and KCNE3 by mutation allows the S4 segment to move down by hyperpolarization.

How the tight interaction between the S1 segment and KCNE3 identified in the current study affects the S4 segment is still up in the air. In the KCNQ1-KCNE3-CaM complex structure, the S4 segment directly interacts with KCNE3 and the S1 segment through its lower part (Sun and MacKinnon, 2020). Therefore, it is reasonable to speculate that the tight interaction between the S1 segment and KCNE3 directly affects the S4 movement upon membrane potential change. However, further mutational analyses are needed to understand how the tight interaction between the S1 segment and KCNE3 changes the S4 movement.

In conclusion, our results demonstrate that tight interaction between the S1 segment of the KCNQ1 channel and KCNE3 is required for retaining the VSD in the intermediate position, probably by preventing the S4 segment from going to the down position, thereby keeping the KCNQ1-KCNE3 channels constitutively active.

Materials and Methods

Expression in *Xenopus laevis* oocytes

The human KCNQ1 (NCBI Accession Number NP_000209.2; WT and mutants) and mouse KCNE3 (NP_001177798; WT and mutants) genes were cloned into the pGEMHE expression vector (Liman et al., 1992). The cRNAs were transcribed using mMESSAGE mMACHINE™ T7 Transcription Kits (Thermo Fisher Scientific, AM1344). Oocytes were surgically removed from female *Xenopus laevis* frogs anesthetized in water containing 0.1% tricaine (Sigma-Aldrich, E10521) for 15-30 min. The oocytes were treated with collagenase (Sigma-Aldrich, C0130) for 6-7 h at room temperature to remove the follicular cell layer. Defolliculated oocytes of similar sizes at stage V or VI were selected, microinjected with 50 nl of cRNA solution (10 ng for KCNQ1 and 1 ng for KCNE3) using a NANOJECT II (Drummond Scientific Co.), and incubated until use at 18 °C in Barth's solution (88 mM NaCl, 1 mM KCl, 2.4 mM $NaHCO_3$, 10 mM HEPES, 0.3 mM $Ca(NO_3)_2$, 0.41 mM $CaCl_2$, and 0.82 mM $MgSO_4$, pH 7.6) supplemented with 0.1% penicillin-streptomycin solution (Sigma-Aldrich, P4333). All experiments were approved by the Animal Care Committee of Jichi Medical University (Japan) under protocol no. 18027-03 and were performed according to guidelines.

Two-electrode voltage clamp

cRNA-injected oocytes were incubated for 2-3 days. Ionic currents were recorded with a two-electrode voltage clamp using an OC-725C amplifier (Warner Instruments) at room temperature. The bath chamber was perfused with Ca^{2+}-free ND96 solution (96 mM NaCl, 2 mM KCl, 2.8 mM $MgCl_2$, 5 mM HEPES, pH 7.6) supplemented with 100 μM $LaCl_3$ to block endogenous hyperpolarization-activated currents (Osteen et al., 2010). The microelectrodes were drawn from borosilicate glass capillaries (Harvard Apparatus, GC150TF-10) using a P-1000 micropipette puller (Sutter Instrument) to a resistance of 0.2–1.0 MΩ and filled with 3 M KCl. Currents were elicited from the holding potential of -90 mV to steps ranging from -100 to +60 mV in +20-mV steps each

for 2 sec with 7.5-sec intervals. Oocytes with a holding current larger than -0.2 µA at -90 mV were excluded from the analysis. Generation of voltage-clamp protocols and data acquisition were performed using a Digidata 1550 interface (Molecular Devices) controlled by pCLAMP 10.7 software (Molecular Devices). Data were sampled at 10 kHz and filtered at 1 kHz.

Voltage dependence analysis

G–V relationships were taken from tail current amplitude at -30 mV fitted using pCLAMP 10.7 software (Molecular Devices) to a single Boltzmann equation:

$$G = G_{min} + (G_{max} - G_{min}) / (1+e^{-zF(V - V_{1/2}) / RT}),$$

where G_{max} and G_{min} are the maximum and minimum tail current amplitudes, respectively, z is the effective charge, $V_{1/2}$ is the half-activation voltage, T is the temperature in degrees Kelvin, F is Faraday's constant, and R is the gas constant. G/G_{max}, which is the normalized tail current amplitude, was plotted against membrane potential for presentation of the G–V relationships.

Voltage-clamp fluorometry

Sample preparation, data acquisition, and data analysis were performed similarly as described previously (Nakajo and Kubo, 2014). cRNA-injected oocytes were incubated for 4-5 days, labeled for 30 min with 5 µM Alexa Fluor™ 488 C_5 maleimide (Thermo Fisher Scientific, A10254) in high potassium KD98 solution (98 mM KCl, 1.8 mM $CaCl_2$, 1 mM $MgCl_2$, 5 mM HEPES, pH 7.6) (Nakajo and Kubo, 2014; Osteen et al., 2010), and washed with Ca^{2+}-free ND96 solution to remove unreacted Alexa probes. The bath chamber was filled with Ca^{2+}-free ND96 solution supplemented with 100 µM $LaCl_3$. The microelectrodes were drawn from borosilicate glass capillaries (Harvard Apparatus, GC150TF-15). Currents were elicited from the holding potential of -100 mV to steps ranging from +60 to -160 mV in -20-mV steps each for 2 sec with 10-sec intervals. Oocytes with a holding current larger than -0.3 µA at -100 mV were excluded from the analysis. Generation of voltage-clamp protocols and data acquisition were performed using a Digidata 1440A interface

(Molecular Devices) controlled by pCLAMP 10.7 software (Molecular Devices). Data were sampled at 10 kHz and filtered at 1 kHz. Fluorescence recordings were performed with a macro zoom microscope MVX10 (Olympus) equipped with a 2x objective lens (MVPLAPO 2XC, NA = 0.5, Olympus), 2x magnification changer (MVX-CA2X, Olympus), GFP filter cube (U-MGFPHQ/XL, Olympus), and an XLED1 LED light source with a BDX (450-495 nm) LED module (Excelitas Technologies). Fluorescence signals were obtained by using a photomultiplier (H10722-110; Hamamatsu Photonics) and digitized at 1 kHz through Digidata1440, filtered at 50 Hz, and recorded using pClamp10 simultaneously with ionic currents. The shutter for the excitation was open during the recording, which induced a continuous decrease of fluorescence due to photobleaching. Therefore, we calculated the bleaching rate for each experiment using the baseline levels of the initial 1100 ms before test pulses of each trace and compensated the fluorescence traces by subtracting the bleached component calculated from each trace's bleaching rate (R), assuming that the fluorescence was linearly decreased. Arithmetic operations were performed with Clampfit software from pClamp10.

[Compensated trace] = [recorded trace] x (1 – (R x [time]) (Nakajo and Kubo, 2014),

where [time] is the time value of the point given by Clampfit. We then normalized the fluorescence traces by setting each baseline level to 1.

VCF analysis

F–V relationships were taken from the fluorescence change from the baseline (ΔF) plotted against membrane potential. ΔF values were then normalized by ΔF_{60mV} for the normalized F-V relationships shown in Figure 5 and figure supplement 19. For KCNQ1 alone, F–V relationships were fitted using Igor Pro software (WaveMatrices Co.) to a single Boltzmann equation:

$$F = F_{min} + (F_{max} - F_{min}) / (1+e^{-zF(V - V_{1/2}) / RT}),$$

where F_{min} and F_{max} are the maximum and baseline fluorescence components, z is the effective

charge for the fluorescence component, $V_{1/2}$ is the half-activation voltage for the fluorescence component, T is the temperature in degrees Kelvin, F is Faraday's constant, and R is the gas constant. For KCNQ1 co-expressed with KCNE3, F–V relationships were fitted using Igor Pro software (WaveMatrices Co.) to a double Boltzmann equation:

$$F = F_{min} + (F_1 - F_{min}) / (1+e^{-z_1F(V - V_{1/2(F1)}) / RT}) + (F_2 - F_1) / (1+e^{-z_2F(V - V_{1/2(F2)}) / RT}),$$

where F_1, F_2 and F_{min} are the first, second, and baseline fluorescence components, z1 and z2 are the effective charges for each fluorescence component, $V_{1/2(F1)}$ and $V_{1/2(F2)}$ are the half-activation voltage for each fluorescence component, T is the temperature in degrees Kelvin, F is Faraday's constant, and R is the gas constant.

Statistical analysis

The data were expressed as means ± s.e.m. Statistical analysis was performed with Student's *t*-test and one-way ANOVA with Dunnett's test for single and multiple comparisons, respectively, with EZR software (Kanda, 2013), and significance was assigned at $P < 0.05$ (*$P < 0.05$, **$P < 0.01$, ***$P < 0.001$).

Data availability

All data generated or analyzed during this study are included in this manuscript and the supplementary information. All experiments were repeated five or more times from at least two batches of oocytes.

Acknowledgments

We thank Dr. Yuichiro Fujiwara (Kagawa University) and the Nakajo laboratory members for their valuable discussions. This work was supported by the Japan Society for the Promotion of Science

(JSPS) KAKENHI (Grant Nos. 19K23833 and 20H03200 to G.K. and 17K08552 and 21K06786 to K.N.), by JICHI MEDICAL UNIVERSITY YOUNG INVESTIGATOR AWARD to G.K., and by The Salt Science Research Foundation (Grant No. 2219) to G.K..

Author details

Go Kasuya

Division of Integrated Physiology, Department of Physiology, Jichi Medical University, Shimotsuke, Japan

Contribution: Conceptualization. Performed the experiments. Analyzed the data. Made structural models and presentations. Wrote the manuscript.

Competing interests: No competing interests declared.

Koichi Nakajo

Division of Integrated Physiology, Department of Physiology, Jichi Medical University, Shimotsuke, Japan

Contribution: Conceptualization. Performed the experiments. Analyzed the data. Wrote the manuscript.

Competing interests: No competing interests declared.

Figure legends

Figure 1. Key residues involved in the interaction between KCNQ1 and KCNE3.

(**A**) Close-up view of the interface between KCNQ1 and KCNE3 in the KCNQ1-KCNE3-CaM complex structure (PDB: 6V00). Three KCNQ1 subunits are colored in blue, green, and gray. A KCNE3 subunit is colored in red. The residues involved in the KCNQ1-KCNE3 interaction are depicted by stick models. The molecular graphics were illustrated with CueMol (http://www.cuemol.org/). (**B, C**) Sequence alignment around the S1 segment of KCNQ1 (B) and the TM segments of KCNE3 and KCNE1 (C). Amino acid sequences were aligned using Clustal Omega and are shown using ESPript3 (Robert and Gouet, 2014). KCNQ1 residues focused on in this work are highlighted with blue dots. KCNE3 residues focused on in this work and "the triplet" (Melman et al., 2002, 2001) are highlighted with red dots and an orange square, respectively. For sequence alignment, human KCNQ1 (HsKCNQ1, NCBI Accession Number: NP_000209), mouse KCNQ1 (MmKCNQ1, NP_032460), chicken KCNQ1 (GgKCNQ1, XP_421022), *Xenopus* KCNQ1 (XlKCNQ1, XP_018111887), human KCNE3 (HsKCNE3, NP_005463), mouse KCNE3 (MmKCNE3, NP_001177798), chicken KCNE3 (GgKCNE3, XP_003640673), *Xenopus* KCNE3 (XlKCNE3 NP_001082346), and human KCNE1 (HsKCNE1, NP_000210) were used.

Figure 2. Functional effects of KCNQ1 S1 mutants on KCNQ1 modulation by KCNE3.

(**A-G**) Representative current traces (A-F) and G-V relationships (G) of KCNQ1 WT with or without KCNE3 WT as well as the F127 mutants with KCNE3 WT. (**H-L**) Representative current traces (H-K) and G-V relationships (L) of the I145 mutants with KCNE3 WT. (**M-S**) Ratios of conductance at -100 mV (G_{-100mV}) and maximum conductance (G_{max}) of KCNQ1 F123 (M), F127 (N), F130 (O), L134 (P), I138 (Q), L142 (R), and I145 (S) mutants with (filled bars) or without (open bars) KCNE3 WT. Error bars indicate ± s.e.m. for n = 10 in (G,L,M-S).

Figure 3. Functional effects of KCNE3 mutants on KCNQ1 modulation by KCNE3.

(**A-G**) Representative current traces (A-F) and G-V relationships (G) of KCNQ1 WT with the KCNE3 S57 mutants. (**H-M**) Representative current traces (H-L) and G-V relationships (M) of KCNQ1 WT with the KCNE3 G73 mutants. (**N-S**) Ratios of conductance at -100 mV (G_{-100mV}) and maximum conductance (G_{max}) of KCNQ1 WT with KCNE3 S57 (N), I61 (O), M65 (P), A69 (Q), G73 (R), and I76 (S) mutants. Error bars indicate ±s.e.m. for *n* = 10 in (G,M,N-S).

Figure 4. Functional restoration of KCNQ1 mutants by KCNE3 mutants

(**A-G**) Representative current traces (A-E), G-V relationships (F), and ratios of conductance at -100 mV (G_{-100mV}) and maximum conductance (G_{max}) (G) of the KCNQ1 F127A mutant with the KCNE3 G73 mutants. (**H-O**) Representative current traces (H-M), G-V relationships (N), and ratios of conductance at -100 mV (G_{-100mV}) and maximum conductance (G_{max}) (O) of the KCNQ1 I145F mutant with the KCNE3 S57 mutants. Error bars indicate ± s.e.m. for *n* = 10 in (F,G,N,O).

Figure 5. Conductance-voltage and fluorescence–voltage relationships for KCNQ1 mutants with KCNE3 mutants.

(**A-E**) Ionic currents (upper row) and fluorescence traces (lower row) of $KCNQ1_{vcf}$ WT-KCNE3 WT (A), $KCNQ1_{vcf}$ F127A-KCNE3 WT (B), $KCNQ1_{vcf}$ F127A-KCNE3 G73L (C), $KCNQ1_{vcf}$ I145F-KCNE3 WT (D), and $KCNQ1_{vcf}$ I145F-KCNE3 S57A (E). (**F-I**) G-V (F,H) and F-V (G,I) relationships of $KCNQ1_{vcf}$ WT-KCNE3 WT, $KCNQ1_{vcf}$ F127A-KCNE3 WT, $KCNQ1_{vcf}$ F127A-KCNE3 G73L, $KCNQ1_{vcf}$ I145F-KCNE3 WT, and $KCNQ1_{vcf}$ I145F-KCNE3 S57A. Error bars indicate ± s.e.m. for *n* = 5 in (F-I).

Figure supplement 1, related to Figure 2. Current traces and G-V relationships of KCNQ1 F123 mutants.

(**A-F**) Representative current traces (A-D) and G-V relationships (E,F) of KCNQ1 F123 mutants with or without KCNE3 WT. Error bars indicate ± s.e.m. for n = 10 in (E,F).

Figure supplement 2, related to Figure 2. Current traces and G-V relationships of KCNQ1 F127 mutants.

(**A-L**) Representative current traces (A-H) and G-V relationships (I-L) of KCNQ1 F127 mutants with or without KCNE3 WT. Error bars indicate ± s.e.m. for n = 10 in (I-L). For clear comparisons, the current traces of KCNQ1 F127 mutants with KCNE3 WT shown in Figure 2C-F are redisplayed here.

Figure supplement 3, related to Figure 2. Current traces and G-V relationships of KCNQ1 F130 mutants.

(**A-L**) Representative current traces (A-H) and G-V relationships (I-L) of KCNQ1 F130 mutants with or without KCNE3 WT. Error bars indicate ± s.e.m. for n = 10 in (I-L).

Figure supplement 4, related to Figure 2. Current traces and G-V relationships of KCNQ1 L134 mutants.

(**A-L**) Representative current traces (A-H) and G-V relationships (I-L) of KCNQ1 L134 mutants with or without KCNE3 WT. Error bars indicate ± s.e.m. for n = 10 in (I-L).

Figure supplement 5, related to Figure 2. Current traces and G-V relationships of KCNQ1 I138 mutants.

(**A-L**) Representative current traces (A-H) and G-V relationships (I-L) of KCNQ1 I138 mutants with or without KCNE3 WT. Error bars indicate ± s.e.m. for *n* = 10 in (I-L).

Figure supplement 6, related to Figure 2. Current traces and G-V relationships of KCNQ1 L142 mutants.

(**A-L**) Representative current traces (A-H) and G-V relationships (I-L) of KCNQ1 L142 mutants with or without KCNE3 WT. Error bars indicate ± s.e.m. for *n* = 10 in (I-L).

Figure supplement 7, related to Figure 2. Current traces and G-V relationships of KCNQ1 I145 mutants.

(**A-L**) Representative current traces (A-H) and G-V relationships (I-L) of KCNQ1 I145 mutants with or without KCNE3 WT. Error bars indicate ± s.e.m. for *n* = 10 in (I-L). For clear comparisons, the current traces of KCNQ1 I145 mutants with KCNE3 WT shown in Figure 2H-K are redisplayed here.

Figure supplement 8, related to Figure 3. Dose-dependent modulation of KCNQ1 by decreasing amounts of KCNE3 WT and mutants.

(**A-F**) Representative current traces (A-E) and G-V relationships (B) of KCNQ1 WT co-expressed with each amount of KCNE3 WT. (**G-L**) Representative current traces (G-K) and G-V relationships (L) of KCNQ1 WT co-expressed with each amount of the KCNE3 S57A mutant. (**M-R**) Representative current traces (M-Q) and G-V relationships (F) of KCNQ1 WT co-expressed with each amount of the KCNE3 G73L mutant. Error bars indicate ± s.e.m. for *n* = 10 in 10 ng KCNQ1

with 1 ng KCNE3 conditions and for *n* = 5 in the other conditions in (F,L,R). For clear comparisons, the current traces of 10 ng KCNQ1 WT with 1 ng KCNE3 WT and mutants shown in Figures 2B, 3B and 3J are redisplayed here.

Figure supplement 9, related to Figure 3. Current traces and G-V relationships of KCNQ1 WT with the KCNE3 I61 mutants.

(**A-F**) Representative current traces (A-E) and G-V relationships (F) of KCNQ1 WT with the KCNE3 I61 mutants. Error bars indicate ± s.e.m. for *n* = 10 in (F).

Figure supplement 10, related to Figure 3. Current traces and G-V relationships of KCNQ1 WT with the KCNE3 M65 mutants.

(**A-G**) Representative current traces (A-F) and G-V relationships (G) of KCNQ1 WT with the KCNE3 M65 mutants. Error bars indicate ± s.e.m. for *n* = 10 in (G).

Figure supplement 11, related to Figure 3. Current traces and G-V relationships of KCNQ1 WT with the KCNE3 A69 mutants.

(**A-F**) Representative current traces (A-E) and G-V relationships (F) of KCNQ1 WT with the KCNE3 A69 mutants. Error bars indicate ± s.e.m. for *n* = 10 in (F).

Figure supplement 12, related to Figure 3. Current traces and G-V relationships of KCNQ1 WT with the KCNE3 I76 mutants.

(**A-F**) Representative current traces (A-E) and G-V relationships (F) of KCNQ1 WT with the KCNE3 I76 mutants. Error bars indicate ± s.e.m. for *n* = 10 in (F).

Figure supplement 13, related to Figure 4. Current traces, G-V relationships, and ratios of conductance of the KCNQ1 F130 mutants with the KCNE3 A69 mutants.

(**A-G**) Representative current traces (A-E), G-V relationships (F), and ratios of conductance at -100 mV (G_{-100mV}) and maximum conductance (G_{max}) (G) of the KCNQ1 F130A mutant with the KCNE3 A69 mutants. (**H-N**) Representative current traces (H-L), G-V relationships (M), and ratios of conductance at -100 mV (G_{-100mV}) and maximum conductance (G_{max}) (N) of the KCNQ1 F130V mutant with the KCNE3 A69 mutants. Error bars indicate ± s.e.m. for *n* = 10 in (F,G,M,N).

Figure supplement 14, related to Figure 4. Current traces, G-V relationships, and ratios of conductance of the KCNQ1 I138 mutants with the KCNE3 M65 mutants.

(**A-H**) Representative current traces (A-F), G-V relationships (G), and ratios of conductance at -100 mV (G_{-100mV}) and maximum conductance (G_{max}) (H) of the KCNQ1 I138A mutant with the KCNE3 M65 mutants. (**I-P**) Representative current traces (I-N), G-V relationships (O), and ratios of conductance at -100 mV (G_{-100mV}) and maximum conductance (G_{max}) (P) of the KCNQ1 I138W mutant with the KCNE3 M65 mutants. Error bars indicate ± s.e.m. for *n* = 10 in (G,H,O,P).

Figure supplement 15, related to Figure 4. Current traces, G-V relationships, and ratios of conductance of the KCNQ1 L142 mutants with the KCNE3 I61 mutants.

(**A-G**) Representative current traces (A-E), G-V relationships (F), and ratios of conductance at -100 mV (G_{-100mV}) and maximum conductance (G_{max}) (G) of the KCNQ1 L142A mutant with the KCNE3 I61 mutants. (**H-N**) Representative current traces (H-L), G-V relationships (M), and ratios of conductance at -100 mV (G_{-100mV}) and maximum conductance (G_{max}) (N) of the KCNQ1 L142W mutant with the KCNE3 I61 mutants. Error bars indicate ± s.e.m. for *n* = 10 in (F,G,M,M).

Figure supplement 16, related to Figure 4. Current traces, G-V relationships, and ratios of conductance of the KCNQ1 I145W mutant with the KCNE3 S57 mutants.

(**A-H**) Representative current traces (A-F), G-V relationships (G), and ratios of conductance at -100 mV (G_{-100mV}) and maximum conductance (G_{max}) (H) of the KCNQ1 I145W mutant with the KCNE3 S57 mutants. Error bars indicate ± s.e.m. for *n* = 10 in (G,H).

Figure supplement 17, related to Figure 5. Conductance-voltage and fluorescence–voltage relationships for KCNQ1 mutants.

(**A-C**) Ionic currents (upper row) and fluorescence traces (lower row) of $KCNQ1_{vcf}$ WT (A), $KCNQ1_{vcf}$ F127A (B), and $KCNQ1_{vcf}$ I145F (C). (**D,E**) G-V (D) and F-V (E) relationships of $KCNQ1_{vcf}$ WT, $KCNQ1_{vcf}$ F127A, and $KCNQ1_{vcf}$ I145F. Error bars indicate ± s.e.m. for *n* = 5 in (D,E).

Table supplement 1, related to Figure 2. Summary of the electrophysiological properties of KCNQ1 WT and mutants with or without KCNE3 WT.

Maximum tail current amplitudes (I_{max}), parameters deduced from the Boltzmann fitting ($V_{1/2}$ and z), and ratios of conductance at -100 mV (G_{-100mV}) and maximum conductance (G_{max}) of KCNQ1 WT and mutants with or without KCNE3 WT. n is the number of experiments.

Table supplement 2, related to Figure 3. Summary of the electrophysiological properties of KCNQ1 WT with KCNE3 mutants.

Maximum tail current amplitudes (I_{max}), parameters deduced from the Boltzmann fitting ($V_{1/2}$ and z), and ratios of conductance at -100 mV (G_{-100mV}) and maximum conductance (G_{max}) of KCNQ1 WT with KCNE3 mutants. n is the number of experiments.

Table supplement 3, related to Figure 4. Summary of the electrophysiological properties of KCNQ1 mutants with KCNE3 mutants.

Maximum tail current amplitudes (I_{max}), parameters deduced from the Boltzmann fitting ($V_{1/2}$ and z), and ratios of conductance at -100 mV (G_{-100mV}) and maximum conductance (G_{max}) of KCNQ1 mutants with KCNE3 mutants. n is the number of experiments.

Table supplement 4, related to Figure 5. Summary of the electrophysiological properties of $KCNQ1_{vcf}$ WT and mutants with or without KCNE3 mutants.

Maximum tail current amplitudes (I_{max}) and parameters deduced from the Boltzmann fitting ($V_{1/2}$ and z) of $KCNQ1_{vcf}$ WT and mutants with or without KCNE3 mutants. n is the number of experiments.

Table supplement 5, related to Figure 5. Summary of the properties of $KCNQ1_{vcf}$ WT and mutants with or without KCNE3 mutants acquired from VCF recordings..

Parameters deduced from the double Boltzmann fitting ($V_{1/2(F1)}$ and $V_{1/2(F2)}$) of $KCNQ1_{vcf}$ WT and mutants with or without KCNE3 mutants. n is the number of experiments.

References

Abbott GW. 2016. KCNE1 and KCNE3: the yin and yang of voltage-gated K+ channel regulation. *Gene* **576**:1–13. doi:10.1016/j.gene.2015.09.059.

Aggarwal SK, MacKinnon R. 1996. Contribution of the S4 segment to gating charge in the Shaker K+ channel. *Neuron* **16**:1169–1177. doi:10.1016/S0896-6273(00)80143-9

Barhanin J, Lesage F, Guillemare E, Fink M, Lazdunski M, Romey G. 1996. KvLQT1 and lsK (minK) proteins associate to form the IKs cardiac potassium current. *Nature* **384**:78–80.

Barro-Soria R, Perez ME, Larsson HP. 2015. KCNE3 acts by promoting voltage sensor activation in KCNQ1. *Proc Natl Acad Sci U S A* **112**:E7286–E7292. doi:10.1073/pnas.1516238112

Barro-Soria R, Ramentol R, Liin SI, Perez ME, Kass RS, Larsson HP. 2017. KCNE1 and KCNE3 modulate KCNQ1 channels by affecting different gating transitions. *Proc Natl Acad Sci U S A* **114**:E7367–E7376. doi:10.1073/pnas.1710335114

Barro-Soria R, Rebolledo S, Liin SI, Perez ME, Sampson KJ, Kass RS, Larsson HP. 2014. KCNE1 divides the voltage sensor movement in KCNQ1/KCNE1 channels into two steps. *Nat Commun* **5**. doi:10.1038/ncomms4750

Bendahhou S, Marionneau C, Haurogne K, Larroque MM, Derand R, Szuts V, Escande D, Demolombe S, Barhanin J. 2005. In vitro molecular interactions and distribution of KCNE family with KCNQ1 in the human heart. *Cardiovasc Res* **67**:529–538. doi:10.1016/j.cardiores.2005.02.014

Catterall WA. 1988. Structure and Function of Voltage-Sensitive Ion Channels. *Science* **242**:50–61. doi:10.1126/science.2459775.

Chung DY, Chan PJ, Bankston JR, Yang L, Liu G, Marx SO, Karlin A, Kass RS. 2009. Location of KCNE1 relative to KCNQ1 in the IKS potassium channel by disulfide cross-linking of substituted cysteines. *Proc Natl Acad Sci U S A* **106**:743–748. doi:10.1073/pnas.0811897106

Fedida D, Hesketh JC. 2001. Gating of voltage-dependent potassium channels. *Prog Biophys Mol Biol*

75:165–199. doi:10.1016/S0079-6107(01)00006-2

Grahammer F, Herling AW, Lang HJ, Schmitt-Gräff A, Wittekindt OH, Nitschke R, Bleich M, Barhanin J, Warth R. 2001. The cardiac K+ channel KCNQ1 is essential for gastric acid secretion. *Gastroenterology* **120**:1363–1371. doi:10.1053/gast.2001.24053

Hou P, Eldstrom J, Shi J, Zhong L, McFarland K, Gao Y, Fedida D, Cui J. 2017. Inactivation of KCNQ1 potassium channels reveals dynamic coupling between voltage sensing and pore opening. *Nat Commun* **8**:1–11. doi:10.1038/s41467-017-01911-8

Jensen MØ, Jogini V, Borhani DW, Leffler AE, Dror RO, Shaw DE. 2012. Mechanism of voltage gating in potassium channels. *Science (80-)* **336**:229–233. doi:10.1126/science.1216533

Kanda Y. 2013. Investigation of the freely available easy-to-use software "EZR" for medical statistics. *Bone Marrow Transplant* **48**:452–458. doi:10.1038/bmt.2012.244

Kang C, Tian C, Sönnichsen FD, Smith JA, Meiler J, George AL, Vanoye CG, Hak JK, Sanders CR. 2008. Structure of KCNE1 and implications for how it modulates the KCNQ1 potassium channel. *Biochemistry* **47**:7999–8006. doi:10.1021/bi800875q

Kroncke BM, Van Horn WD, Smith J, Kang C, Welch RC, Song Y, Nannemann DP, Taylor KC, Sisco NJ, George AL, Meiler J, Vanoye CG, Sanders CR. 2016. Structural basis for KCNE3 modulation of potassium recycling in epithelia. *Sci Adv* **2**. doi:10.1126/sciadv.1501228

Larsson HP, Baker OS, Dhillon DS, Isacoff EY. 1996. Transmembrane movement of the Shaker K+ channel S4. *Neuron* **16**:387–397. doi:10.1016/S0896-6273(00)80056-2

Liman ER, Hess P. 1991. Voltage-sensing residues in the S4 region of a mammalian K+ channel. *Nature* **353**:752–756. doi:10.1038/353752a0

Liman ER, Tytgat J, Hess P. 1992. Subunit stoichiometry of a mammalian K+ channel determined by construction of multimeric cDNAs. *Neuron* **9**:861–871. doi:10.1016/0896-6273(92)90239-a

Logothetis DE, Movahedi S, Satler C, Lindpaintner K, Nadal-Ginard B. 1992. Incremental reductions of

positive charge within the S4 region of a voltage-gated K+ channel result in corresponding decreases in gating charge. *Neuron* **8**:531–540. doi:10.1016/0896-6273(92)90281-H

Long SB, Campbell EB, MacKinnon R. 2005. Crystal structure of a mammalian voltage-dependent Shaker family K + channel. *Science* **309**:897–903. doi:10.1126/science.1116269

Mannuzzu LM, Moronne MM, Isacoff EY. 1996. Direct physical measure of conformational rearrangement underlying potassium channel gating. *Science* **271**:213–216. doi:10.1126/science.271.5246.213

Melman YF, Domènech A, De la Luna S, McDonald T V. 2001. Structural Determinants of KvLQT1 Control by the KCNE Family of Proteins. *J Biol Chem* **276**:6439–6444. doi:10.1074/jbc.M010713200

Melman YF, Krumerman A, McDonald T V. 2002. A single transmembrane site in the KCNE-encoded proteins controls the specificity of KvLQT1 channel gating. *J Biol Chem* **277**:25187–25194. doi:10.1074/jbc.M200564200

Nakajo K. 2019. Gating modulation of the KCNQ1 channel by KCNE proteins studied by voltage-clamp fluorometry. *Biophys physicobiology* **16**:121–126. doi:10.2142/biophysico.16.0_121

Nakajo K, Kubo Y. 2014. Steric hindrance between S4 and S5 of the KCNQ1/KCNE1 channel hampers pore opening. *Nat Commun* **5**. doi:10.1038/ncomms5100

Nakajo K, Kubo Y. 2011. Nano-environmental changes by KCNE proteins modify KCNQ channel function. *Channels* **5**:1–6. doi:10.4161/chan.5.5.16468

Nakajo K, Kubo Y. 2007. KCNE1 and KCNE3 Stabilize and/or Slow Voltage Sensing S4 Segment of KCNQ1 Channel. *J Gen Physiol* **130**:269–281. doi:10.1085/jgp.200709805

Nakajo K, Nishino A, Okamura Y, Kubo Y. 2011. KCNQ1 subdomains involved in KCNE modulation revealed by an invertebrate KCNQ1 orthologue. *J Gen Physiol* **138**:521–535. doi:10.1085/jgp.201110677

Noda M, Shimizu S, Tanabe T, Takai T, Kayano T, Ikeda T, Takahashi H, Nakayama H, Kanaoka Y, Minamino N, Kangawa K, Matsuo H, Raftery MA, Hirose T, Inayama S, Hayashida H, Miyata T, Numa

S. 1984. Primary structure of Electrophorus electricus sodium channel deduced from cDNA sequence. *Nature* **312**:121–127. doi:10.1038/312121a0

Osteen JD, Barro-Soria R, Robey S, Sampson KJ, Kass RS, Larsson HP. 2012. Allosteric gating mechanism underlies the flexible gating of KCNQ1 potassium channels. *Proc Natl Acad Sci U S A* **109**:7103–7108. doi:10.1073/pnas.1201582109

Osteen JD, Gonzalez C, Sampson KJ, Iyer V, Rebolledo S, Larsson HP, Kass RS. 2010. KCNE1 alters the voltage sensor movements necessary to open the KCNQ1 channel gate. *Proc Natl Acad Sci U S A* **107**:22710–22715. doi:10.1073/pnas.1016300108

Papazian DM, Timpe LC, Jan YN, Jan LY. 1991. Alteration of voltage-dependence of Shaker potassium channel by mutations in the S4 sequence. *Nature* **349**:305–310. doi:10.1038/349305a0

Preston P, Wartosch L, Günzel D, Fromm M, Kongsuphol P, Ousingsawat J, Kunzelmann K, Barhanin J, Warth R, Jentsch TJ. 2010. Disruption of the K+ channel β-subunit KCNE3 reveals an important role in intestinal and tracheal Cl- transport. *J Biol Chem* **285**:7165–7175. doi:10.1074/jbc.M109.047829

Robert X, Gouet P. 2014. Deciphering key features in protein structures with the new ENDscript server. *Nucleic Acids Res* **42**:320–324. doi:10.1093/nar/gku316

Rocheleau JM, Kobertz WR. 2008. KCNE peptides differently affect voltage sensor equilibrium and equilibration rates in KCNQ1 K+ channels. *J Gen Physiol* **131**:59–68. doi:10.1085/jgp.200709816

Sanguinetti MC, Curran ME, Zou A, Shen J, Spector PS, Atkinson DL, Keating MT. 1996. Coassembly of K(V)LQT1 and minK (IsK) proteins to form cardiac I(Ks) potassium channel. *Nature* **384**:80–83. doi:10.1038/384080a0

Schroeder BC, Waldegger S, Fehr S, Bleich M, Warth R, Greger R, Jentsch TJ. 2000. A constitutively open potassium channel formed by KCNQ1 and KCNE3. *Nature* **403**:196–199. doi:10.1038/35003200

Sun J, MacKinnon R. 2020. Structural Basis of Human KCNQ1 Modulation and Gating. *Cell* **180**:340–347. doi:10.1016/j.cell.2019.12.003

Takumi T, Ohkubo H, Nakanishi S. 1988. Cloning of a membrane protein that induces a slow voltage-gated potassium current. *Science* **242**:1042–1045. doi:10.1126/science.3194754

Taylor KC, Kang PW, Hou P, Yang N Du, Kuenze G, Smith JA, Shi J, Huang H, White KM, Peng D, George AL, Meiler J, McFeeters RL, Cui J, Sanders CR. 2020. Structure and physiological function of the human KCNQ1 channel voltage sensor intermediate state. *Elife* **9**:1–31. doi:10.7554/eLife.53901

Van Horn WD, Vanoye CG, Sanders CR. 2011. Working model for the structural basis for KCNE1 modulation of the KCNQ1 potassium channel. *Curr Opin Struct Biol* **21**:283–291. doi:10.1016/j.sbi.2011.01.001

Wang Y, Eldstrom J, Fedida D. 2020. Gating and Regulation of KCNQ1 and KCNQ1 + KCNE1 Channel Complexes. *Front Physiol* **11**:1–21. doi:10.3389/fphys.2020.00504

Xu L, Jiang M, Hsu KL, Zhang M, Tseng GN. 2008. KCNQ1 and KCNE1 in the IKs channel complex make state-dependent contacts in their extracellular domains. *J Gen Physiol* **131**:589–603. doi:10.1085/jgp.200809976

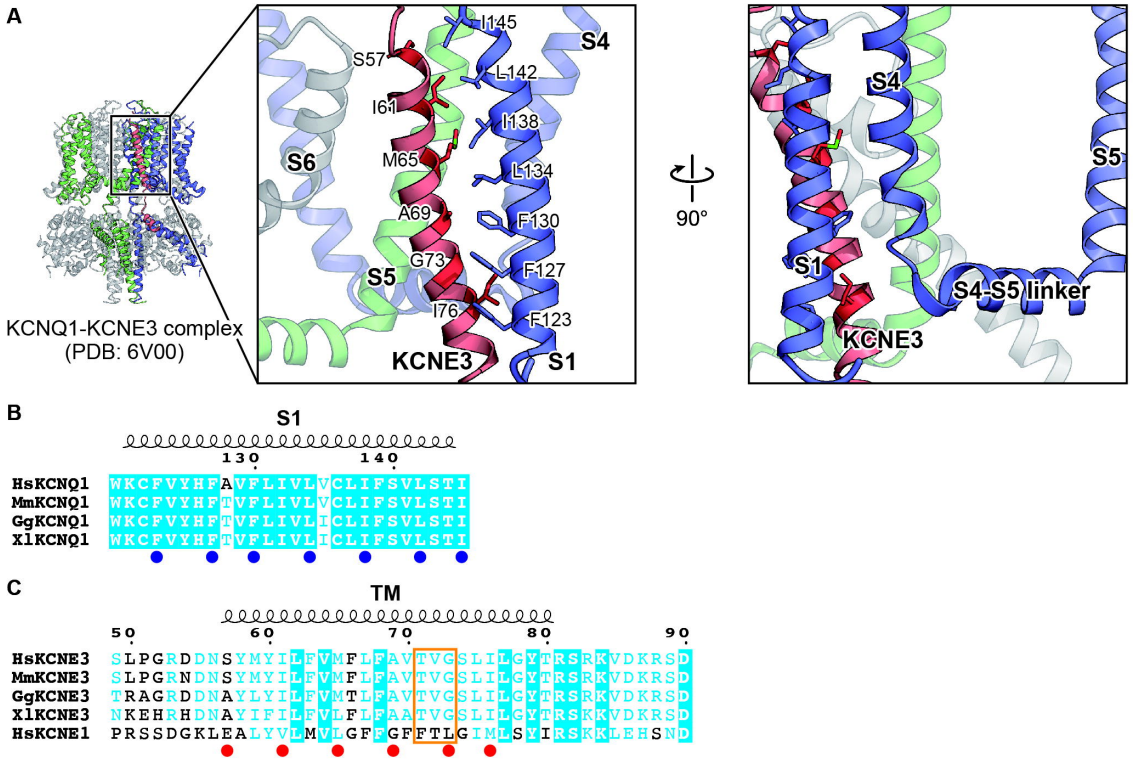
A
KCNQ1-KCNE3 complex
(PDB: 6V00)
S57
I145
S4
L142
I61
I138
S6
M65
L134
A69
F130
G73
F127
S5
I76
F123
KCNE3
S1
90°
S4
S5
S1
S4-S5 linker
KCNE3
B
S1
130
140
HsKCNQ1 WKCFVYHFAVFLIVLVCLIFSVLSTI
MmKCNQ1 WKCFVYHFTVFLIVLVCLIFSVLSTI
GgKCNQ1 WKCFVYHFTVFLIVLICLIFSVLSTI
XlKCNQ1 WKCFVYHFTVFLIVLICLIFSVLSTI
C
TM
50
60
70
80
90
HsKCNE3 SLPGRDDNSYMYILFVMFLFAVTVGSLILGYTRSRKVDKRSD
MmKCNE3 SLPGRNDNSYMYILFVMFLFAVTVGSLILGYTRSRKVDKRSD
GgKCNE3 TRAGRDDNAYLYILFVMTLFAVTVGSLILGYTRSRKVDKRSD
XlKCNE3 NKEHRHDNAYIFILFVLFLFAATVGSLILGYTRSKKVDKRSD
HsKCNE1 PRSSDGKLEALYVLMVLGFFGFFTLGIMLSYIRSKKLEHSND

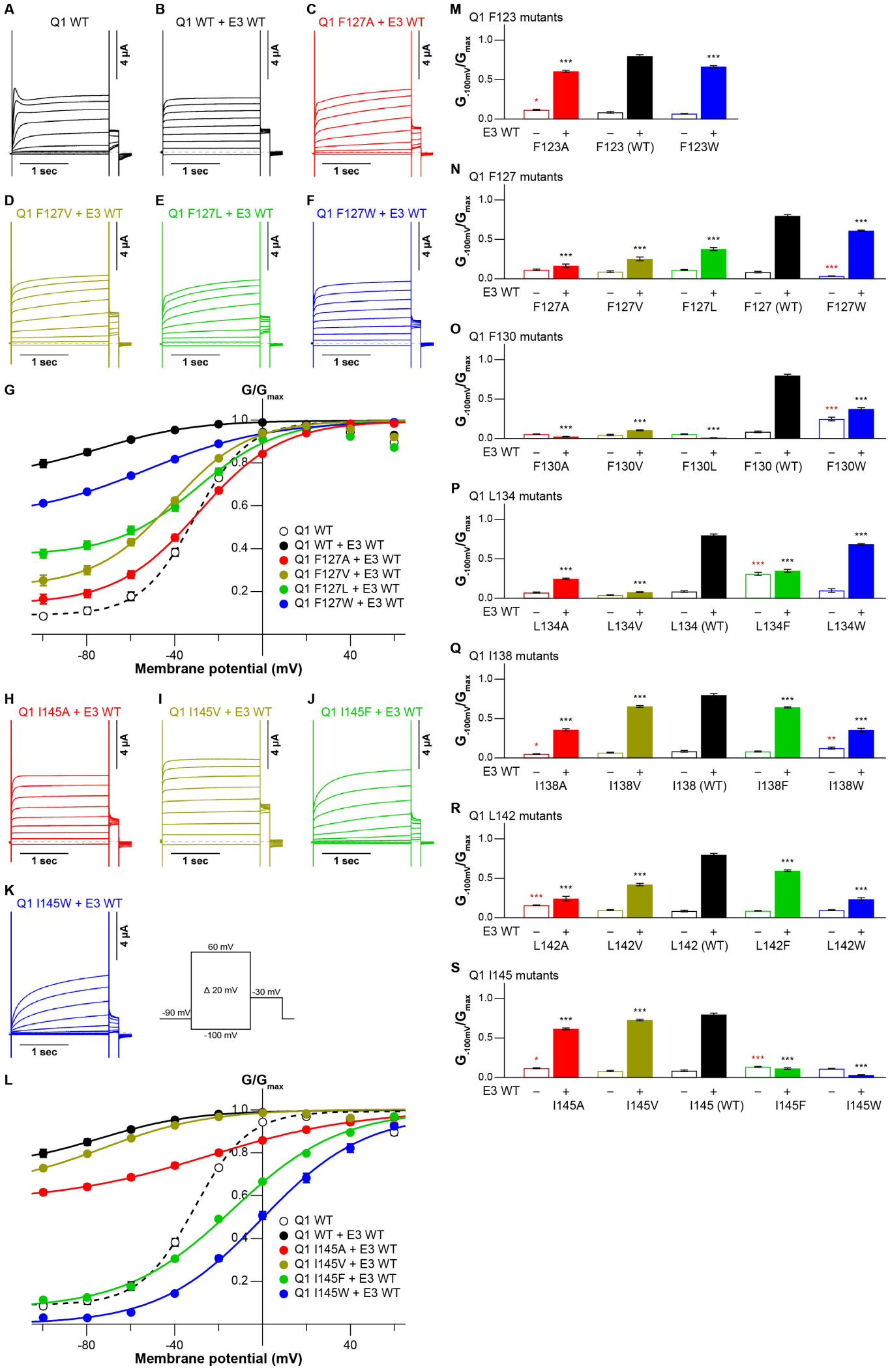
A
Q1 WT
B
Q1 WT + E3 WT
C
Q1 F127A + E3 WT
D
Q1 F127V + E3 WT
E
Q1 F127L + E3 WT
F
Q1 F127W + E3 WT
4 µA
1 sec
G
G/Gmax
Q1 WT
Q1 WT + E3 WT
Q1 F127A + E3 WT
Q1 F127V + E3 WT
Q1 F127L + E3 WT
Q1 F127W + E3 WT
Membrane potential (mV)
H
Q1 I145A + E3 WT
I
Q1 I145V + E3 WT
J
Q1 I145F + E3 WT
K
Q1 I145W + E3 WT
60 mV
Δ 20 mV
-30 mV
-90 mV
-100 mV
L
Q1 WT
Q1 WT + E3 WT
Q1 I145A + E3 WT
Q1 I145V + E3 WT
Q1 I145F + E3 WT
Q1 I145W + E3 WT
Membrane potential (mV)
M
Q1 F123 mutants
G-100mV/Gmax
E3 WT
F123A
F123 (WT)
F123W
N
Q1 F127 mutants
F127A
F127V
F127L
F127 (WT)
F127W
O
Q1 F130 mutants
F130A
F130V
F130L
F130 (WT)
F130W
P
Q1 L134 mutants
L134A
L134V
L134 (WT)
L134F
L134W
Q
Q1 I138 mutants
I138A
I138V
I138 (WT)
I138F
I138W
R
Q1 L142 mutants
L142A
L142V
L142 (WT)
L142F
L142W
S
Q1 I145 mutants
I145A
I145V
I145 (WT)
I145F
I145W

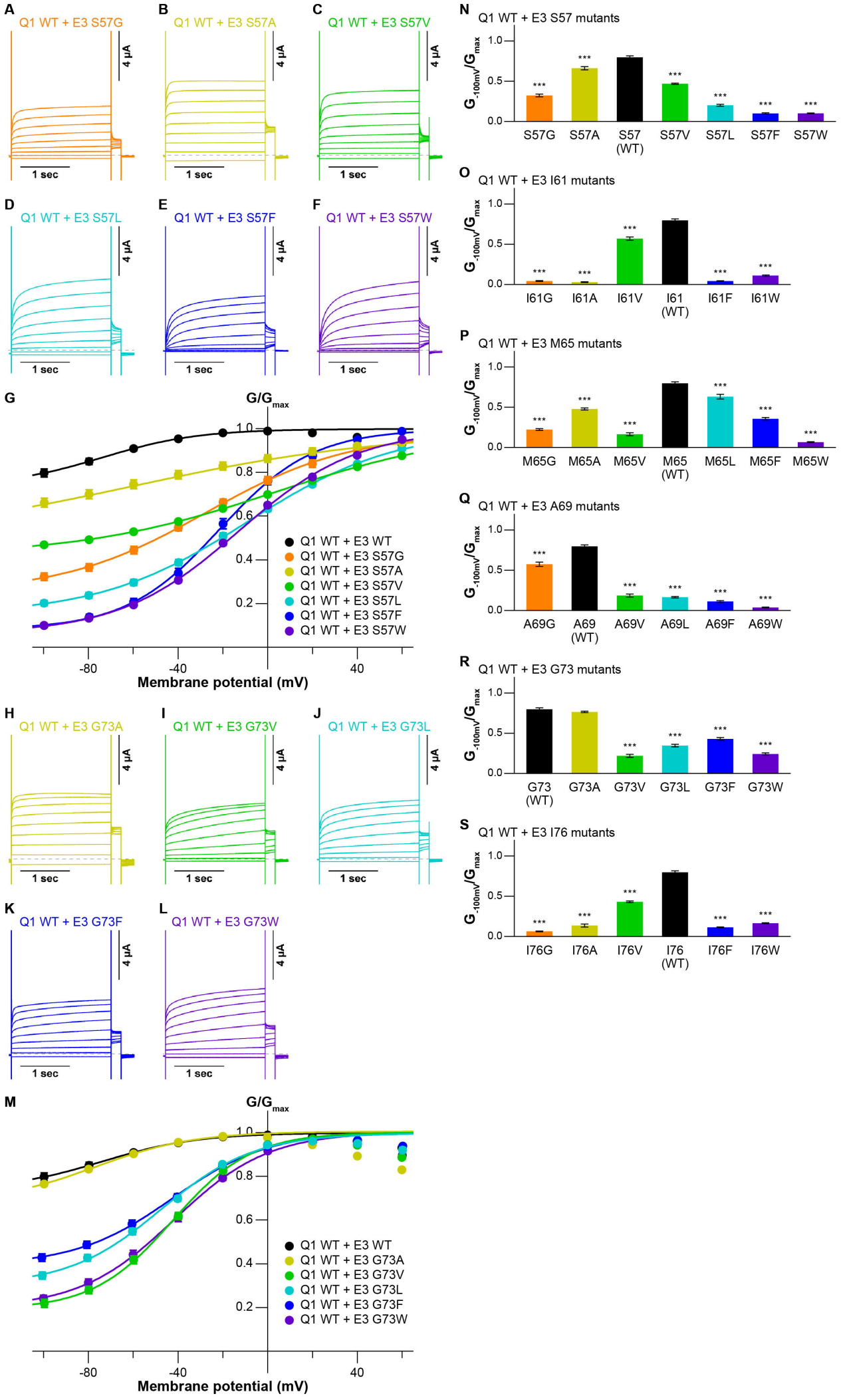
A
Q1 WT + E3 S57G
B
Q1 WT + E3 S57A
C
Q1 WT + E3 S57V
D
Q1 WT + E3 S57L
E
Q1 WT + E3 S57F
F
Q1 WT + E3 S57W
4 µA
1 sec
G
G/Gmax
Q1 WT + E3 WT
Q1 WT + E3 S57G
Q1 WT + E3 S57A
Q1 WT + E3 S57V
Q1 WT + E3 S57L
Q1 WT + E3 S57F
Q1 WT + E3 S57W
Membrane potential (mV)
H
Q1 WT + E3 G73A
I
Q1 WT + E3 G73V
J
Q1 WT + E3 G73L
K
Q1 WT + E3 G73F
L
Q1 WT + E3 G73W
M
Q1 WT + E3 WT
Q1 WT + E3 G73A
Q1 WT + E3 G73V
Q1 WT + E3 G73L
Q1 WT + E3 G73F
Q1 WT + E3 G73W
Membrane potential (mV)
N
Q1 WT + E3 S57 mutants
G-100mV/Gmax
S57G
S57A
S57 (WT)
S57V
S57L
S57F
S57W
O
Q1 WT + E3 I61 mutants
I61G
I61A
I61V
I61 (WT)
I61F
I61W
P
Q1 WT + E3 M65 mutants
M65G
M65A
M65V
M65 (WT)
M65L
M65F
M65W
Q
Q1 WT + E3 A69 mutants
A69G
A69 (WT)
A69V
A69L
A69F
A69W
R
Q1 WT + E3 G73 mutants
G73 (WT)
G73A
G73V
G73L
G73F
G73W
S
Q1 WT + E3 I76 mutants
I76G
I76A
I76V
I76 (WT)
I76F
I76W

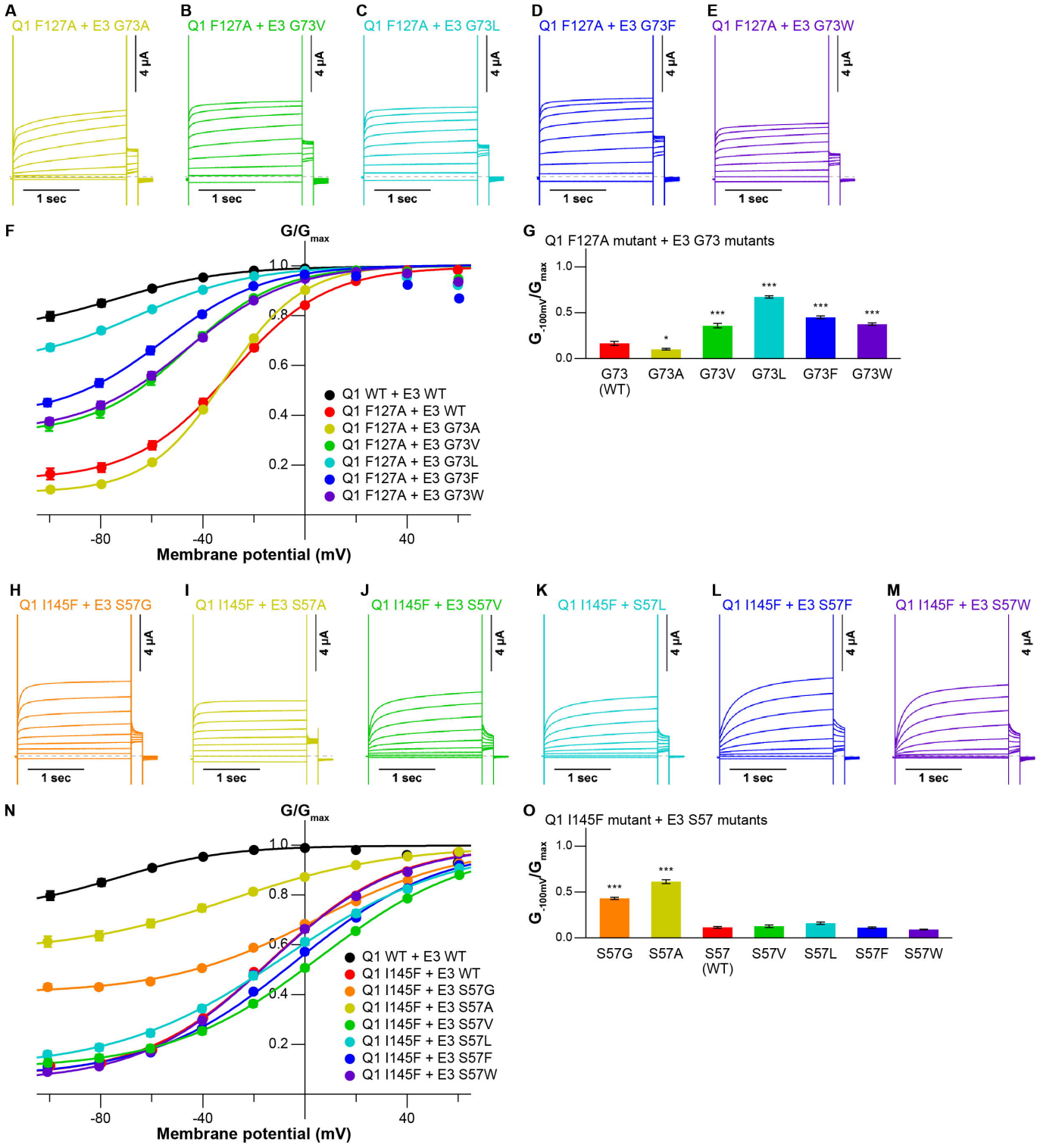
A
Q1 F127A + E3 G73A
B
Q1 F127A + E3 G73V
C
Q1 F127A + E3 G73L
D
Q1 F127A + E3 G73F
E
Q1 F127A + E3 G73W
4 µA
1 sec
F
G/Gmax
Q1 WT + E3 WT
Q1 F127A + E3 WT
Q1 F127A + E3 G73A
Q1 F127A + E3 G73V
Q1 F127A + E3 G73L
Q1 F127A + E3 G73F
Q1 F127A + E3 G73W
Membrane potential (mV)
G
Q1 F127A mutant + E3 G73 mutants
G-100mV/Gmax
G73 (WT)
G73A
G73V
G73L
G73F
G73W
H
Q1 I145F + E3 S57G
I
Q1 I145F + E3 S57A
J
Q1 I145F + E3 S57V
K
Q1 I145F + S57L
L
Q1 I145F + E3 S57F
M
Q1 I145F + E3 S57W
N
Q1 WT + E3 WT
Q1 I145F + E3 WT
Q1 I145F + E3 S57G
Q1 I145F + E3 S57A
Q1 I145F + E3 S57V
Q1 I145F + E3 S57L
Q1 I145F + E3 S57F
Q1 I145F + E3 S57W
Membrane potential (mV)
O
Q1 I145F mutant + E3 S57 mutants
S57G
S57A
S57 (WT)
S57V
S57L
S57F
S57W

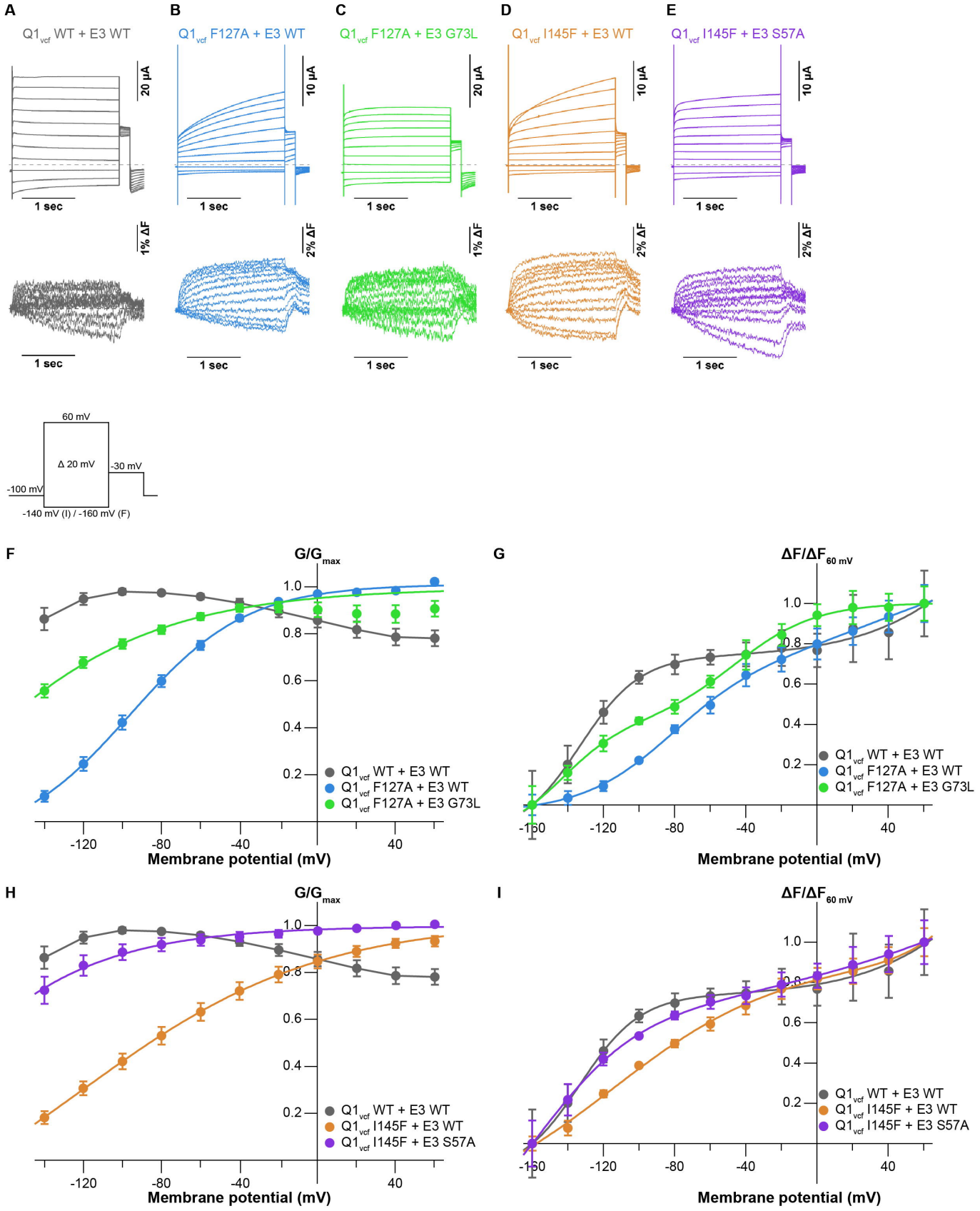
A
Q1vcf WT + E3 WT
B
Q1vcf F127A + E3 WT
C
Q1vcf F127A + E3 G73L
D
Q1vcf I145F + E3 WT
E
Q1vcf I145F + E3 S57A
20 µA
10 µA
1 sec
1% ΔF
2% ΔF
60 mV
Δ 20 mV
-30 mV
-100 mV
-140 mV (I) / -160 mV (F)
F
G/Gmax
Q1vcf WT + E3 WT
Q1vcf F127A + E3 WT
Q1vcf F127A + E3 G73L
Membrane potential (mV)
G
ΔF/ΔF60 mV
H
Q1vcf I145F + E3 WT
Q1vcf I145F + E3 S57A
I